A rational design of $NaLnF_4@Cu_{2-x}S$ hybrid theranostic nanoplatform for *in vivo* through-skull brain imaging beyond 1500 nm and photothermal therapy

Mingyang Jiang, Xiaolong Li, Zhenluan Xue, Youbin Li, Songjun Zeng, Hongrong Liu*, and Jianhua Hao**

Prof. S. J. Zeng, M. Y. Jiang, Dr. X. L. Li, Z. L. Xue, Z. M. Deng, Prof. H. R. Liu

College of Physics and Information Science and Key Laboratory of Low-dimensional Quantum Structures and Quantum Control of the Ministry of Education, Synergetic Innovation Center for Quantum Effects and Applications, Hunan Normal University, Changsha, Hunan 410081 (China)

E-mail: ***songjunz@hunnu.edu.cn*** **,** ***hrliu@hunnu.edu.cn***

Prof. J. H. Hao

Department of Applied Physics, The Hong Kong Polytechnic University, Hong Kong (China)

E-mail: ***jh.hao@polyu.edu.hk***

Keywords: lanthanide nanomaterials, theranostic nanoprobes, NIR-II optical imaging, brain blood vessel imaging, photothermal therapy

Abstract:

Theranostic nanoprobes with combination of highly sensitive optical bioimaging and photothermal therapy (PTT) are considered as advanced tools for improving the detection precision and imaging-guided hyperthermal therapy efficacy of tumor in biomedical area. Compared with the traditional visible/first near-infrared (NIR-I) light-emitting optical probe, the nanoprobe capable of generating the second near-infrared (NIR-II) emission is emerged as the next generation advanced optical imaging technique for high-sensitivity, high spatial/time resolution bioimaging owing to the remarkably reduced photon scattering losses. However, the multifunctional theranostic nanoplatform integrated the new advanced NIR-II optical imaging and PTT has not yet been explored. Herein, we demonstrate a general strategy of designing theranostic nanoplatform holding synergistic NIR-II optical bioimaging and photothermal function via *in-situ* growth of $Cu_{2-x}S$ quantum dots on the lanthanide nanorods. The as-prepared $NaLnF_4$:Yb/Er@$Cu_{2-x}S$ hybrid nanoprobes with core-satellite nanostructure present excellent NIR-II emission centered at 1525 nm, highly stable photothermal effect and good biocompatibility. These designed theranostic nanoprobes are successfully utilized for NIR-II optical imaging, small tumor detection (5 mm in diameter) and PTT for the first time. More importantly, non-invasive brain vessel visualization with high spatial resolution (44.2 μm) through scalp and skull without craniotomy was demonstrated. Therefore, these results pave the way of designing new multifunction theranostic nanoplatform for highly sensitive NIR-II optical-guided tumor detection, non-invasive blood vessel imaging and PTT.

The development of a single theranostic nanoprobe by integrating imaging and PTT has attracted enormous research interest owing to their potential and powerful applications in biological labeling, tumor early detection, and tumor therapy.[1-11] Among different imaging modalities, fluorescence-based optical imaging as a noninvasive imaging technique has drawn immense attention in the imaging-guided therapy platform due to the advantages of high accuracy, high sensitivity, absence of radiation and fast feedback.[12] However, the traditional optical imaging in the visible (400-750 nm) and first near-infrared (NIR-I, 750-900 nm) range affords very limited tissue penetration and low spatial/temporal resolution owing to the large photons absorption and scattering.[13] Recently, optical bioimaging in the second near-infrared window (NIR-II, 1000-1700 nm) has been emerged as the next generation of fluorescence imaging method, owing to the significantly decreased photon scattering losses (1000-fold reduction) than the conventional visible/NIR-I imaging, subsequently resulting in unprecedented improvement in imaging sensitive, depth, and resolution.[14-15] Thus, the development of fluorescence probe working in NIR-II window is significant importance for designing highly sensitive theranostic nanoplatform.

Up to now, only a few agents capable of generating NIR-II emission are explored for NIR-II imaging, including organic fluorophores,[16-17] quantum dots (QDs),[18] single-walled carbon nanotubes (SWNTs)[14] and lanthanide-based luminescent nanomaterials.[19] However, the organic fluorophores present relatively low quantum yield and serious photobleaching effect, which limits their wide-spread application in bioimaging area.[20] While, QDs commonly contain toxic elements such as lead, mercury, cadmium and arsenic, which are also harmful and unsuitable for *in vivo* application.[21] Although, SWNTs have been developed and used for *in vivo* NIR-II imaging, it still

remains several drawbacks, such as optimal excitation outside the NIR-II window near 650 nm, broad-band emission spanning >300 nm, and large size distribution ranging from several to hundreds of nanometers, impeding their application in multispectral bioimaging and size-dependent biodistribution study.[19] [22] Recently, the lanthanide-based luminescent materials once again attract increased interest because of their ability of generating high efficient down-conversion NIR-II emissions. However, most of the lanthanide-based luminescent materials have been developed as upconversion (UC) imaging agents for NIR-I optical bioimaging,[23] the simultaneous superior NIR-II emission under laser excitation has nearly been ignored. Compared with the QDs and SWNT-based probes, the lanthanide materials possess many advantages, including narrow-band emission, low toxicity, high efficient down-conversion NIR-II emission, and well-controlled size distribution. Therefore, development of the lanthanide-based NIR-II imaging agent is emerged for designing the multifunctional theranostic nanoprobes.

On the other hand, PTT as a noninvasive therapy technology, employing photoabsorbing nanoparticles or molecules to convert near-infrared light to heat energy for ablating tumor, shows great potential for improving the therapeutic accuracy and reducing side effect of normal tissues.[24] So far, a number of NIR-absorbing nanomaterials have been developed as photothermal agents. In particular, $Cu_{2-x}S$ nanoparticles are considered as promising PTT agent owing to the advantages of low production cost, high thermal stability, high photothermal conversion efficiency and low toxicity.[25] Therefore, development of highly sensitive theranostic nanoplatform by integrating lanthanide-based NIR-II agent with $Cu_{2-x}S$-based PTT QDs is urgently required, however, it is still a great challenge. Although an electrostatic attraction method [3,26-27] was developed for integrating

lanthanide-based NIR-I agent with $Cu_{2-x}S$, the *in-situ* growth of multifunction nanoplatform integrated the new advanced lanthanide-based NIR-II optical imaging and $Cu_{2-x}S$-based PTT has not yet been reported.

Here, we demonstrate a general *in-situ* growth strategy of realizing multifunctional $NaLnF_4@Cu_{2-x}S$ core-satellite nanostructure as the therapeutic nanoplatform. The achieved *in vitro* and *in vivo* NIR-II imagings demonstrated that these $NaLnF_4@Cu_{2-x}S$ probes may exhibit superior detection sensitivity, successfully realizing the small tumor diagnosis. Meanwhile, the through-skull non-invasive brain vessel imaging without craniotomy was presented. In addition, these $NaLnF_4@Cu_{2-x}S$ probes also possessed high photothermal effect without obvious side-effect. These features make the designed $NaLnF_4@Cu_{2-x}S$ nanocomposite promising and ideal theranostic nanoplatform for highly sensitive bioimaging and high efficiency PTT.

A general *in-situ* growth method of constructing the multifunctional core-satellite typed $NaLnF_4@Cu_{2-x}S$ nanostructure is demonstrated in **Scheme 1**. As a proof of concept, theranostic $NaYF_4$:Yb/Er@$Cu_{2-x}S$ hybrid nanostructure is selected as example because of its well-known high efficiency NIR-II emission of the core $NaYF_4$:Yb/Er and high efficient photothermal conversion of $Cu_{2-x}S$. The $NaYF_4$:Gd/Yb/Er core was first synthesized by oleic acid (OA)-assistant hydrothermal method. Then, the hydrophobic OA-modified core was transferred to the hydrophilic one with negatively charged poly acrylic acid (PAA) ligand by ligand exchange method. After that, the negatively charged core can absorb Cu^{2+} with positive charge by electrostatic interaction. Finally, an *in-situ* growth of $Cu_{2-x}S$ QDs on the core surface was realized by adding sulfur source to form the core-satellite typed structure.

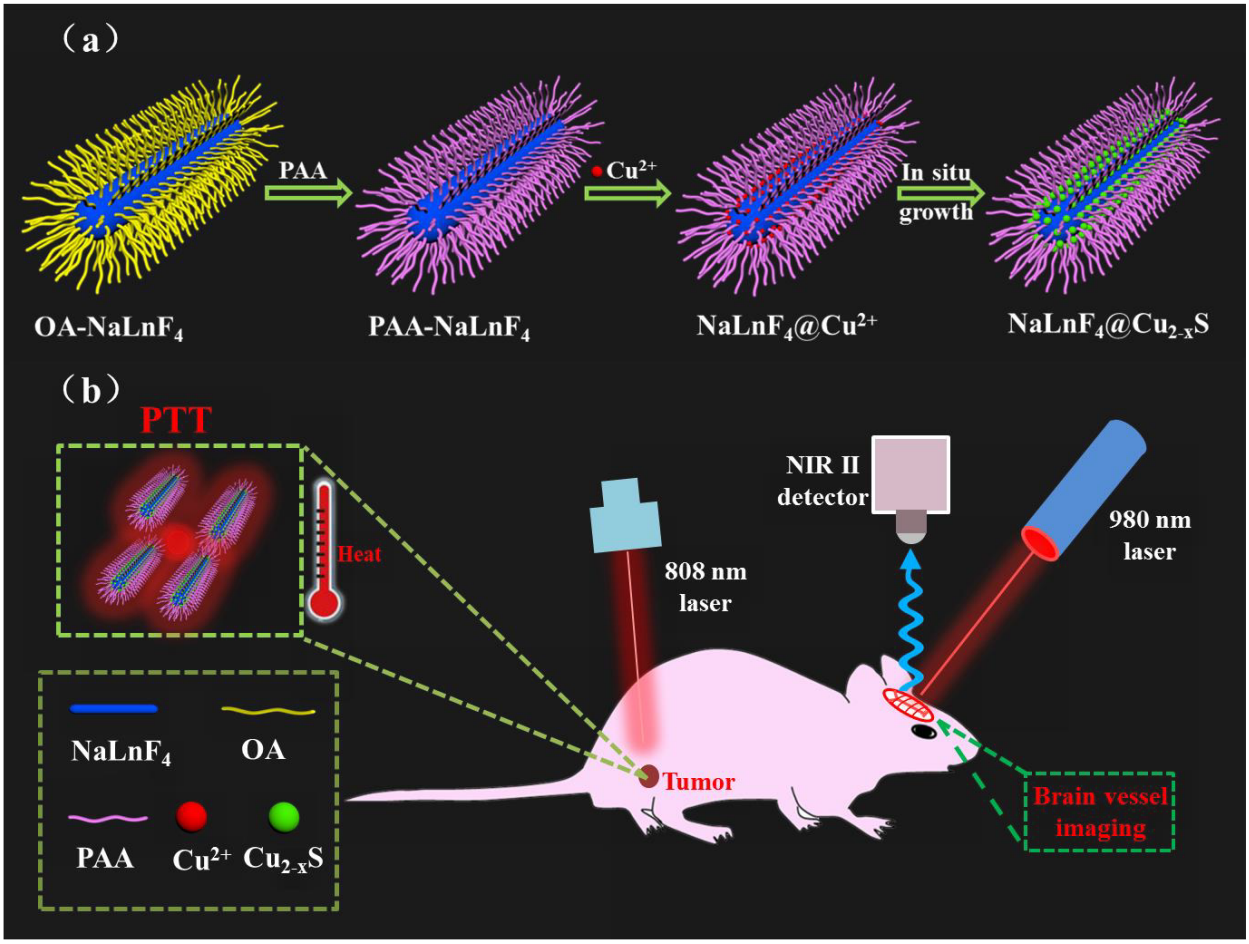

Scheme 1. a) Schematic illustration of designing $NaLnF_4@Cu_{2-x}S$ theranostic probe; b) schematic diagram of $NaYF_4$:Yb,Gd,Er@$Cu_{2-x}S$ nanocomposites as NIR-II nanoprobes and PTT agents for NIR-II imaging-guided PTT.

Figure 1a shows the transmission electron microscopy (TEM) image of the OA-capped $NaYF_4$:Gd/Yb/Er core, indicating the formation of highly uniform rod-like shape. After *in-situ* growth, as shown in **Figure 1b**, the ultra-small $Cu_{2-x}S$ QDs are successfully grown on the surface of the $NaYF_4$:Gd/Yb/Er core, unambiguously validating the formation of the core-satellite typed nanostructure by *in-situ* growth method. High resolution TEM (HRTEM) of a single nanocomposite (**Figure 1c**) reveals two main lattice distances of 0.300 and 0.275 nm, matching well with the (101)

crystal plane of $Cu_{2-x}S$ and the (200) crystal plane of $NaYF_4$, respectively. To further reveal the *in-situ* growth of $Cu_{2-x}S$ on $NaYF_4$ core, the digital photography (**Figure 1d**) of the water solution containing PAA-$NaYF_4$, $NaYF_4@Cu^{2+}$, pure $CuCl_2$ and $NaYF_4@Cu_{2-x}S$ before/after centrifugation is observed. As shown in **Figure 1d**, when adding Cu^{2+} into the PAA-$NaYF_4$ solution, the color was changed from colorless to blue and the Cu^{2+} was dispersed evenly in the water. After centrifugation, compared with the pure PAA-$NaYF_4$ and $CuCl_2$ water solution samples, the color of the precipitated sample was changed from black to blue by adding Cu^{2+}, which unambiguously indicated that the added Cu^{2+} was successfully grafted on the surface of PAA-$NaYF_4$ to form $NaYF_4@Cu^{2+}$ composites via electrostatic interaction. After *in-situ* growth by adding sulfur source, the color of the $NaYF_4@Cu_{2-x}S$ water solution was changed, and after centrifugation the color of the $NaYF_4@Cu_{2-x}S$ precipitation was also changed from blue to black. And no blue color was observed in water solution and precipitated sample, indicating all of the grafted Cu^{2+} ions were successfully turned into $Cu_{2-x}S$ QDs by in-situ growth. XPS analysis (**Figure 1e**) was also performed for validating the formation of $NaYF_4@Cu_{2-x}S$ structure. As demonstrated, after in-situ growth of $Cu_{2-x}S$, besides the signals of Na, Y, Gd, F，a new Cu signal was detected in $NaYF_4@Cu_{2-x}S$ sample, further verifying the growth of $Cu_{2-x}S$ on the surface of the $NaYF_4$ core.

To reveal the optical properties, the UC and DC NIR-II spectra were studied with 980 nm laser excitation. As shown in **Figure 1f** and **Supplementary Fig. S1**, both the $NaYF_4$:Gd/Yb/Er and $NaYF_4$:Gd/Yb/Er@$Cu_{2-x}S$ samples can not only present green 521/540 nm and red 654 nm UC emission, but also hold strong NIR-II emission centered at 1525 nm. The 521/540 and 654 nm UC and 1525 nm DC emissions are ascribed to the $^2H_{11/2}$ /$^4S_{3/2}$ $^4I1_{5/2}$, $^4F_{9/2}$ $^4I1_{5/2}$ and $^4I1_{3/2}$

$^4I1_{5/2}$ electronic transitions of Er^{3+} (**Figure 1g**), respectively.

To shed more light on the versatility of the *in-situ* growth method, we have prepared some other $NaLnF_4@Cu_{2-x}S$ nanocomposites. For example, $NaLuF_4@Cu_{2-x}S$ and $NaYbF_4@Cu_{2-x}S$ hybrid nanostructures were prepared by using the same method. Obviously, the morphology and optical properties of $NaLuF_4@Cu_{2-x}S$ and $NaYbF_4@Cu_{2-x}S$ were in accordance with the case of $NaYF_4@Cu_{2-x}S$, as shown in **Supplementary Fig. S2, S3** and **S4**. These findings reveal that our developed *in-situ* growth strategy can be extended to other material systems, which has the potential to become a general method for designing core-satellite nanohybrid structure.

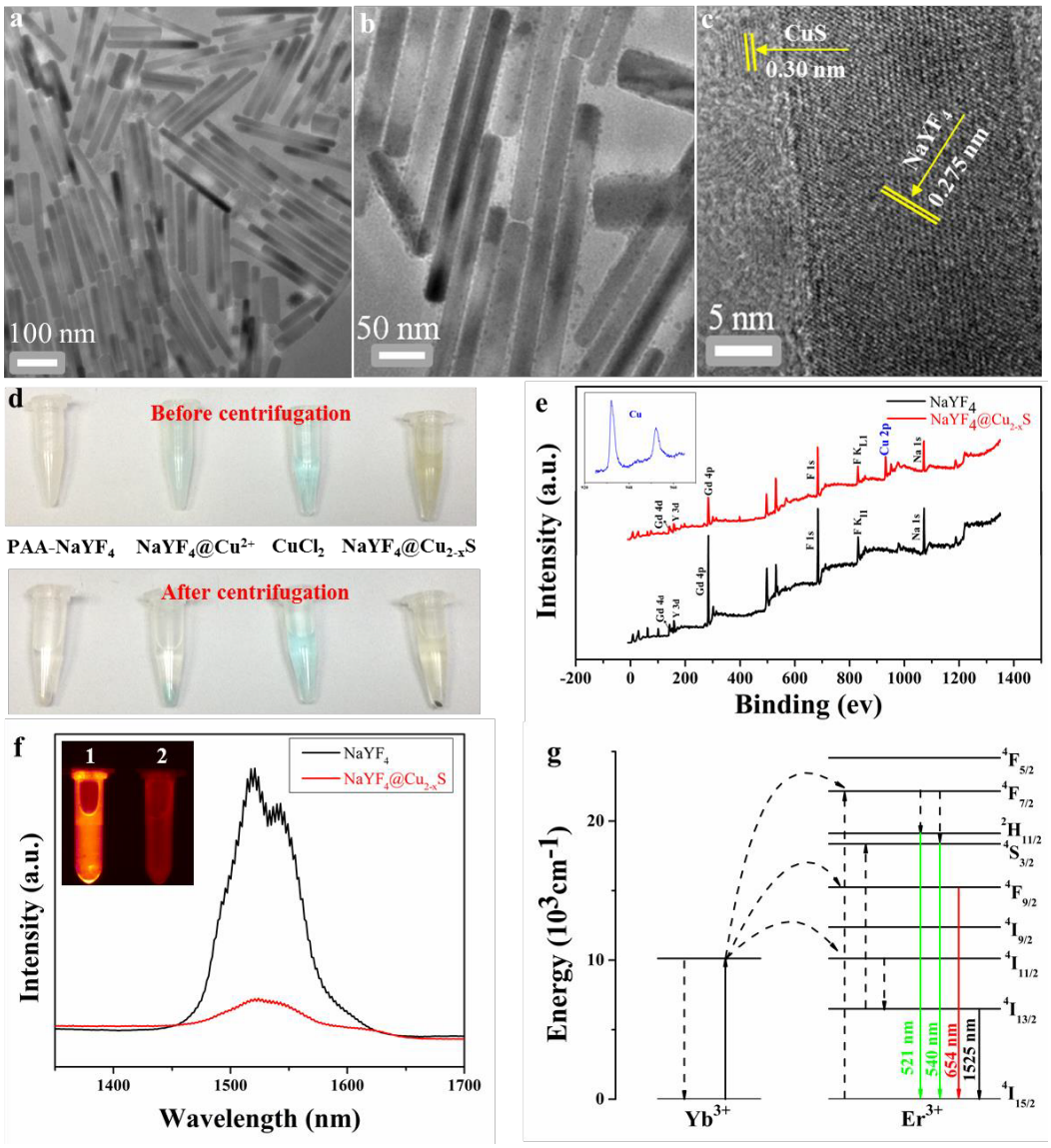

Figure 1. a-b) TEM images of OA-$NaYF_4$ and PAA-$NaYF_4$@$Cu_{2-x}S$, respectively. c) The HRTEM image of a single $NaYF_4$@$Cu_{2-x}S$ nanocrystal. d) The photographs of the PAA-$NaYF_4$, $NaYF_4$@Cu^{2+}, $CuCl_2$, $NaYF_4$@$Cu_{2-x}S$ solutions before/after centrifugation. e) XPS of $NaYF_4$ and $NaYF_4$@$Cu_{2-x}S$. f) The DC NIR-II emission of the $NaYF_4$ and $NaYF_4$@$Cu_{2-x}S$ samples, the inset shows the NIR-II images of the $NaYF_4$ and $NaYF_4$@$Cu_{2-x}S$ solutions. g) Schematic diagram of energy level between Yb^{3+} and Er^{3+}.

NIR-II fluorescence imaging has drawn great attention due to its minimal autofluorescence

from tissue and organ as well as negligible scattering losses and high light penetration depth. To evaluate the real-time *in vivo* NIR-II imaging ability by using the multifunction $NaYF_4@Cu_{2-x}S$ nanocomposites, a small mouse was intravenously injected with the multifunction $NaYF_4@Cu_{2-x}S$ nanoprobes. (2 mg/ml, 150 μL). As shown in **Supplementary Fig. S5a**, a remarkable NIR-II fluorescence signal in the liver region was observed after 1 h treatment, and the signal intensity was increased and reached the maximum intensity after 8 h post-injection. Subsequently, after 8 h injection, the signal was gradually reduced. To assess the biodistribution of $NaYF_4@Cu_{2-x}S$ in the mouse, the organs including liver, spleen, heart, lung, and kidney from the injected mouse was used for *ex vivo* NIR II imaging. As presented in **Supplementary Fig. S5 b**, NIR-II signals were observed in liver and spleen, demonstrating the efficient uptake of $NaYF_4@Cu_{2-x}S$ in the liver and spleen tissues, which belonged to the reticuloendothelial system. The average NIR-II luminescence intensity (**Supplementary Fig. S6)** indicated that the $NaYF_4@Cu_{2-x}S$ nanoprobes were also mainly accumulated in the liver and spleen. The above results demonstrated the $NaYF_4@Cu_{2-x}S$ nanohybrids were promising nanoprobs for *in vivo* imaging. To further demonstrate the optical imaging-guided tumor detection, the HeLa tumor-bearing mouse was selected as the experimental model. After intravenous injection of $NaYF_4@Cu_{2-x}S$ for 4 h, the fluorescent signal in tumor (**Figure 2a**) was weak and the signal was localized mainly in the mouse liver region. The signal in tumor was increased slowly and reached the maximum after 48 h. After 48 h, the signal of tumor region was gradually decreased, validating the long-term tumor visualization. To further confirm tumor detection, the *ex vivo* tumor imaging was performed (**Figure 2b and 2c**) and a significant NIR-II signal was detected at tumor site, further elucidating the successful uptake of probes in

tumor. More importantly, the tumor size was evaluated to be 5 mm, revealing the efficient NIR-II optical imaging-guided small tumor diagnosis. The NIR-II signal intensity evolution (**Figure 2d**) in tumor sites was also assessed, demonstrating the similar changing trend with *in vivo* bioimaging. These findings demonstrate that our designed $NaYF_4@Cu_{2-x}S$ hybrid probes present relative long-time retention in tumor region, which can improve the tumor detection accuracy and benefit for PTT (**Figure. 2a**). Therefore, it is expected that the designed $NaYF_4@Cu_{2-x}S$ nanocomposites with high-performance NIR-II emission are ideal probes for early diagnosis of small tumor.

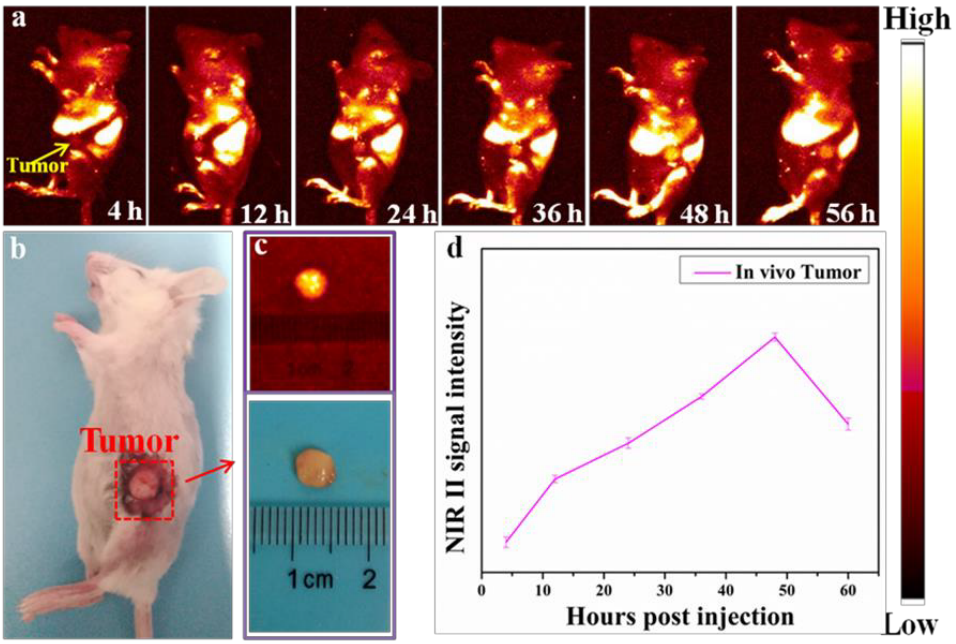

Figure 2. a) *In vivo* NIR-II optical bioimaging of HeLa tumor-bearing mouse after intravenous injection of PAA-$NaYF_4@Cu_{2-x}S$. b) A digital photograph of a HeLa tumor-bearing mouse. c) A digital picture of isolated tumor and the corresponding *ex vivo* NIR-II optical imaging. d) Average intensity of NIR-II signal of tumor based on *in vivo* NIR-II optical bioimaging.

High spatial resolution non-invasive brain vessel imaging has been emerged as an indispensable tool for diagnosing cerebrovascular diseases, measuring blood flow, and analyzing

changes in blood vessel walls.[28] In order to prove the feasibility in practical vessel imaging application, the through-skull non-invasive NIR-II fluorescence imaging of mouse's brain was performed (**Figure 3a**) with field of view (FOV) of 26 mm×21 mm (640×521, 41 μm/pixel) . The mouse head (with hair shaved off) was imaged without craniotomy (**Figure 3b**). Under the excitation of 980 nm laser, the high resolution brain vessel imaging clearly showed the main venule and arteriole vessels of brain. And the inferior cerebral vein, superior sagittal sinus, and transverse sinus depths (marked by 1, 2, and 3 in **Figure 3c**) under the scalp skin are also visualized. Moreover, many tiny capillary vessels can also be distinguished, indicating the high spatial resolution brain vessel imaging. To further study the vascular bifurcations, the intensity profiles (**Figure 3h-k**) along the red, green, blue, and purple lines (marked in **Figure 3d-g**) were plotted. Due to the inevitable scattering and absorbance from the organs and biotissues, the full width at half maximum (FWHM) was used to represent the vessel's diameter. Therefore, the corresponding vessel widths were evaluated to be from 44.2 μm to 97.1 μm by Gaussian-fitted method. These results indicated that the designed $NaYF_4@Cu_{2-x}S$ nanocomposites were ideal probes for high resolution brain blood vessel imaging.

To further test the capacity for high resolution blood vessel imaging, the abdominal imaging of the mouse was performed. As shown in the **Supplementary Fig. S7**, the abdomen blood vessel was also identified with high resolution. Small vessels with 88.97 and 104.45 μm measured by the Gaussian-fitting of the intensity profiles were achieved. These findings validate that our developed $NaYF_4@Cu_{2-x}S$ nanocomposites are promising probes for non-invasive high spatial resolution blood vessel imaging.

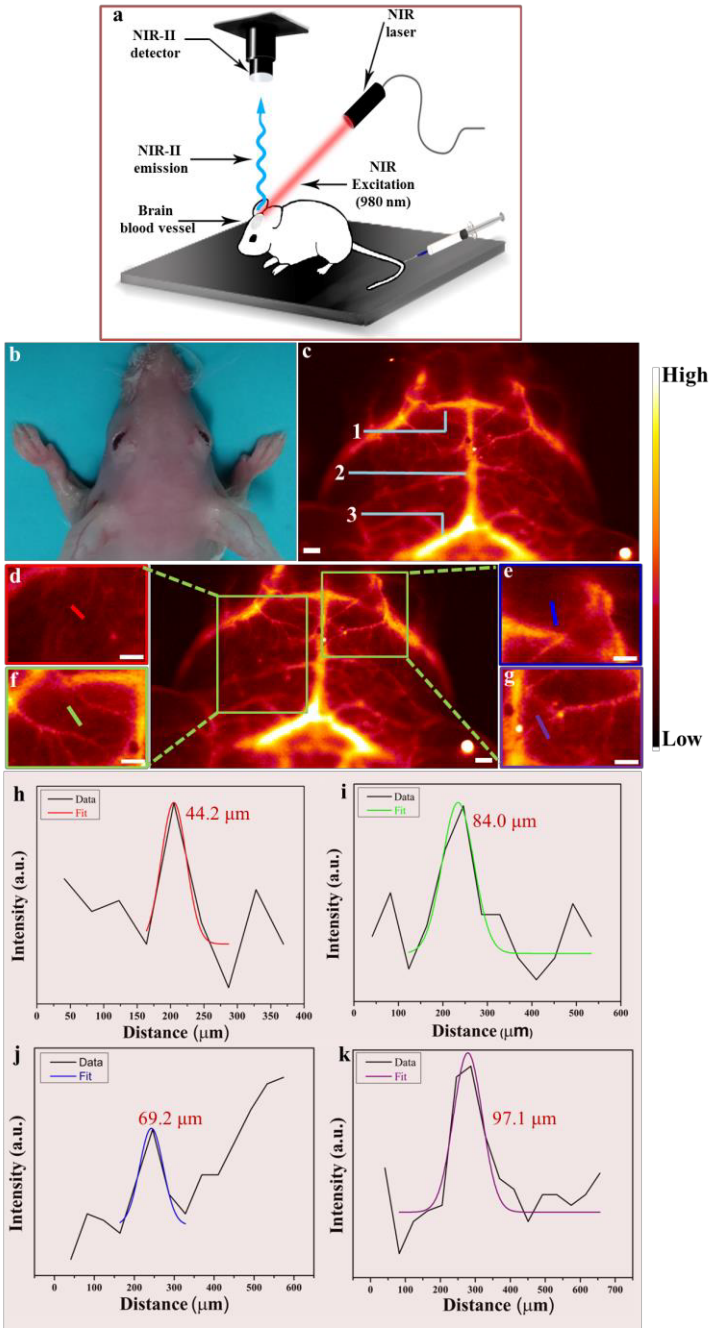

Figure 3. a) Schematically showing the NIR-II fluorescence images of the mouse head. b) A digital image of the mouse head without hair. c) Through-skull non-invasive brain blood vessel image with a FOV of 26 mm × 21 mm. The inferior cerebral vein, superior sagittal sinus and transverse sinus are denoted with 1, 2 and 3. d, e, f, g) are the corresponding amplified image taken from rectangle

region. h-k) The intensity profiles Gaussian fitting results along red, blue, green, and purple lines marked in d, e, f and g, respectively. Scale bar = 0.1 mm.

Owing to the *in-situ* growth of $Cu_{2-x}S$ QDs on the surface of $NaLnF_4$ nanorods, the $NaYF_4$@$Cu_{2-x}S$ nanocomposites can not only present aforementioned NIR-II imaging but also hold efficient photothermal effect. As shown in **Figure 4a**, compared with $NaYF_4$ precursor, the $NaYF_4$@$Cu_{2-x}S$ nanocomposites exhibit a strong absorbance peak in the NIR region, making them suitable for PTT under NIR laser excitation. To confirm the potential PTT application of the $NaYF_4$@$Cu_{2-x}S$ nanocomposites, the temperatures of the $NaYF_4$@$Cu_{2-x}S$ solutions (0.1 mM) were measured under the irradiation of the 808 nm laser with different power densities of 1.0 W/cm^2 and 0.55 W/cm^2. As shown in **Figure 4b**, the temperature was increased from 26 ℃ to 45 ℃ under 1.0 W/cm^2 irradiation, which was higher than the one under 0.55 W/cm^2 laser irradiation. To further investigate the photothermal effect, the pure water and various concentrations (0.1, 0.075, 0.05 mM) of $NaYF_4$@$Cu_{2-x}S$ solutions were irradiated under 808 nm lasers with power density of 1.0 W/cm^2. The heating curves (**Figure 4 c,d**) demonstrated that the temperature was highly depended on the concentration of $NaYF_4$@$Cu_{2-x}S$ solution. High concentration and large laser power can facilitate the increase of the temperature. Moreover, after 10 min irradiation, the temperature of the $NaYF_4$@$Cu_{2-x}S$ solution (0.1 mM) can be improved to 45 ℃, while, the temperature of the pure water is only increased 3℃, indicating the high performance photothermal conversion efficiency of the $NaYF_4$@$Cu_{2-x}S$ nanocomposites.

In addition to this, the photothermal stability of the $NaYF_4$@$Cu_{2-x}S$ nanocomposites was also

studied. The $NaYF_4@Cu_{2-x}S$ aqueous solution (0.05 mM, 2mL) was first irradiated with 808 nm laser (1.0 W/cm^2) until obtain a steady-state temperature. Then the solution was cooled down by turning off the laser. Finally, the heating-cooling process was carried out for four cycles and the temperature change was shown in **Figure 4e**. An almost equal temperature of 12 ℃ was increased during the heating-cooling process, suggesting the high photothermal stability of the $NaYF_4@Cu_{2-x}S$ nanocomposites. In addition, infrared thermal images (**Figure 4f**) also visually validate the high photothermal performance of the $NaYF_4@Cu_{2-x}S$ nanocomposites. Based on the above analysis, the $NaYF_4@Cu_{2-x}S$ nanocomposites present excellent photothermal effect and distinct stability, which are suitable photothermal agents for PTT.

To evaluate the PTT effect of $NaYF_4@Cu_{2-x}S$ *in vivo*, the HeLa tumor-bearing mice were divided into three groups: group I, PBS + subcutaneous injection; group II, $NaYF_4@Cu_{2-x}S$ + subcutaneous injection; group III, $NaYF_4@Cu_{2-x}S$ + intravenous injection. Subsequently, the HeLa tumor-bearing mice from all groups were irradiated with 808 nm laser irradiation (1.0 W/cm^2 for 10 min). The temperature of the tumor-bearing mice from groups II and III increased rapidly and finally reached about 42 ℃ in 10 min, which can kill the tumor with little side effect for normal cells. However, the temperature of the group I (control group) only increased 5℃ **(Figure. 4g)**. To further investigate the tumor-ablation effect, the HeLa tumor-bearing mouse was exposed under the 808 nm laser for 10 min every day. After 22 days irradiation, the tumor in the mouse was almost disappeared and the mouse was still alive (**Figure. 4h**), proving the effective tumor-ablation effect. These findings successfully demonstrate the high photothermal conversion performance and efficient PTT of the $NaYF_4@Cu_{2-x}S$ nanocomposites, making them become an excellent theranostic

nanoplatform for nanomedicine applications.

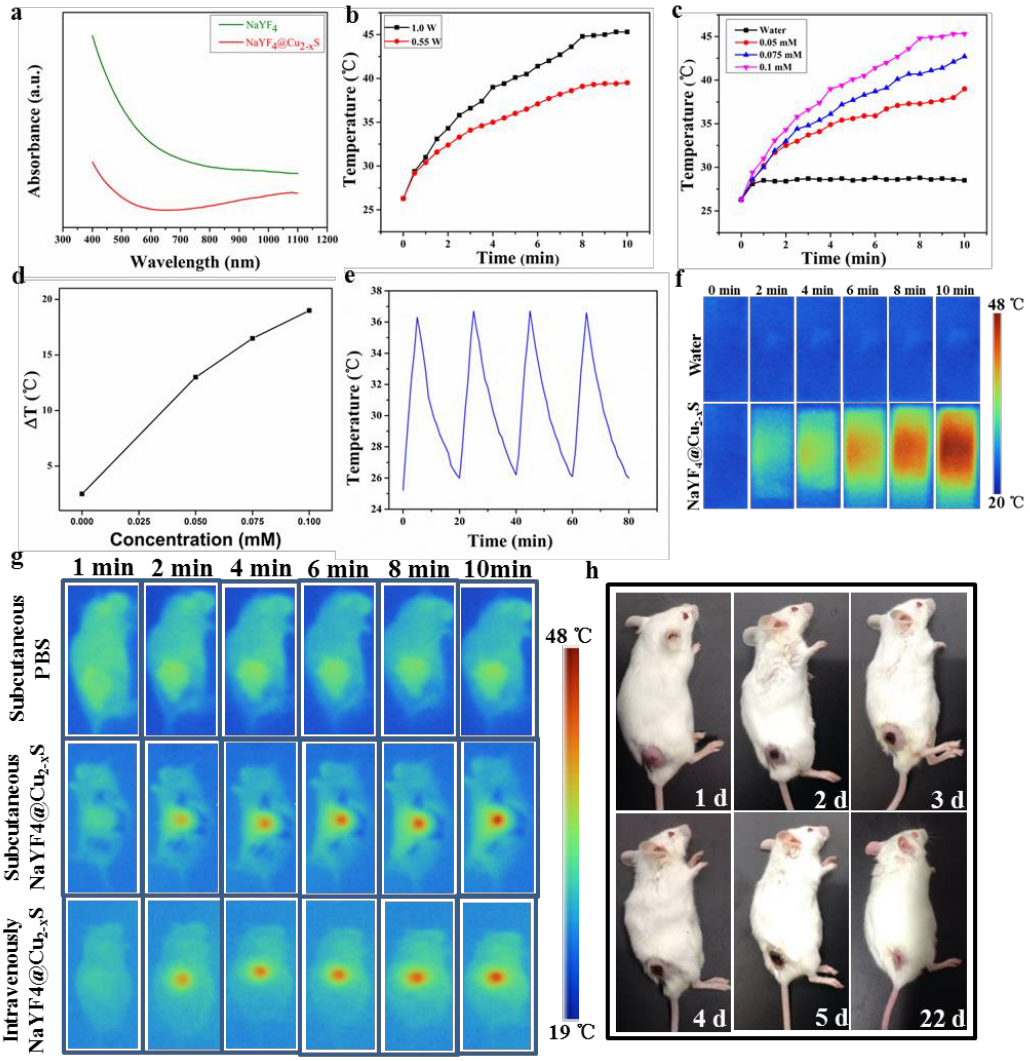

Figure 4. a) UV-Vis-NIR absorbance spectrum of $NaYF_4@Cu_{2-x}S$ nanocrystallines in water. b) Temperature change curves of $NaYF_4@Cu_{2-x}S$ solutions under irradiation with different powers of 808 nm laser. c) Temperature evolution of water and $NaYF_4@Cu_{2-x}S$ solutions with different concentrations. d) Plot of temperature change (□T) versus the concentration of $NaYF_4@Cu_{2-x}S$ solutions. e) Temperature change of $NaYF_4@Cu_{2-x}S$ solutions under four irradiation/cooling cycles with 808 nm laser. f) Thermal infrared images of $NaYF_4@Cu_{2-x}S$ nanocrystallines under 808 nm

laser irradiation. g) Thermal images of the three HeLa tumor-bearing mice under 808 nm laser irradiation after subcutaneous injection of $NaYF_4@Cu_{2-x}S$, PBS and intravenous injection of $NaYF_4@Cu_{2-x}S$. h) Digital image of the tumor mouse during the therapy process.

To further assess the *in vivo* toxicity of the designed $NaLnF_4@C_{2-x}S$ nanoprobe, histological analyses of the main organs (heart, liver, spleen, lung and kidney) from mice at 3/7 days after treatment were performed. As shown in **Supplementary Fig. S8**, the hematoxylin and eosin (H&E) stained tissue sections indicated no obvious histopathological abnormalities or lesions compared with the control group. These evaluation results suggest that $NaLnF_4@Cu_{2-x}S$ nanoprobes present low toxicity *in vivo* and hold a great promise for theranostic applications.

In summary, a general *in-situ* growth strategy of combining PTT-based $Cu_{2-x}S$ and NIR-II emitting $NaLnF_4$ nanorods to form an integrative $NaLnF_4@Cu_{2-x}S$ theranostic nanoplatform was demonstrated for the first time. The $NaLnF_4@Cu_{2-x}S$ probes exhibited superior NIR-II emission beyond 1500 nm, and were successfully used for optical-guided small tumor detection (5 mm in diameter). More importantly, non-invasive brain vessel imaging with high spatial resolution (down to 44.2 μm) without craniotomy was also achieved by using this new NIR-II probe. It should be noted that the achieved spatial resolution of 44.2 μm is closed to the limited resolution of the current imaging FOV of 26 mm×21 mm (640× 512, 41 μm/pixel). Apart from the excellent NIR-II bioimaging, the designed $NaLnF_4@Cu_{2-x}S$ nanoplatform also presents high efficient 808 nm laser-activated PTT effect. Therefore, these findings open up the opportunity of designing high sensitivity theranostic nanoprobes with combination of the next generation NIR-II optical imaging

technique and PTT for simultaneous early tumor diagnosis and therapy.

Supporting Information

Supporting Information is available from the Wiley Online Library or from the author.

Acknowledgment

This work was supported by the National Natural Science Foundation of China (No. 21671064), specialized research Fund for the Doctoral Program of Higher Education of China (No. 20114301120006), Scientific Research Fund of Hunan Provincial Education Department (13B062), and the Hunan Provincial Innovation Foundation for Postgraduate (CX2017B223).

References

[1] L. Cheng, K. Yang, Y. G. Li, J. H. Chen, C. Wang, M. W. Shao, S. T. Lee, Z. Liu, *Angew. Chem.* **2011**, *123*, 7523.

[2] F. He, G. X. Yang, P. P. Yang, Y. X. Yu, R. C. Lv, C. X. Li, Y. L. Dai, S. L. Gai, J. Lin, *Adv. Funct. Mater.* **2015**, *25*, 3966.

[3] Q. F. Xiao, X. P. Zheng, W. B. Bu, W. Q. Ge, S. J. Zhang, F. Chen, H. Y. Xing, Q. G. Ren, W. P. Fan, K. L. Zhao, Y. Q. Hua, J. L. Shi, *J. Am. Chem. Soc.* **2013**,*135*,13041.

[4] X. J. Zhu, W. Feng, J. Chang, Y. W. Tan, J. C. Li, M. Chen, Y. Sun, F. Y. Li, *Nat. Commun.* **2016**, *7*, 10437.

[5] J. T. Xu, A. Gulzar, Y. H. Liu, H. T. Bi, S. L. Gai, B. Liu, D. Yang, F. He, P. P. Yang, *Small* **2017**, *13*, 1701841.

[6] C. L. Chen, C. G. Li, Z. Shi, *Adv. Sci*. **2016**, *3*, 1600029.

[7] F. Y. Liu, X. X. He, Z. Lei, L. Liu, J. P. Zhang, H. P. You, H. M. Zhang, Z. X. Wang, *Adv. Healthcare Mater.* **2014**, *4*, 559.

[8] Y. H. Wang, H. G. Wang, D. P. Liu, S. Y. Song, X. Wang, H. J. Zhang, *Biomaterials* **2013**, 34, 7715.

[9] X. Ding, J. H. Liu, D. P. Liu, J. Q. Li, F. Wang, L. J. Li, Y. H. Wang, S. Y. Song, H. J. Zhang, *Nano. Res.* **2017**, *10,* 3434.

[10] Z. Y. Hou, K. R. Deng, C. X. Li, X. R. Deng, H. Z. Lian, Z. Y. Cheng, D. Y. Jin, J. Lin, *Biomaterials* **2016**, *101*, 32.

[11] B. Liu, C. X. Li, P. P. Yang, Z. Y. Hou, J. Lin, *Adv. Mater.* **2016**, *29*, 1605434.

[12] a) Z. G. Yi, W. Lu, H. R. Liu, S. J. Zeng, *Nanoscale* **2015**, *7*, 542; b) M. Bejia, C. A. M. Afonso, J. M. G. Martinho, *Chem. Soc. Rev.* **2009**, *38*, 2410; c) B. N. G. Giepmans, S. R. Adams, M. H. Ellisman, R. Y. Tsien, *Science* **2006**, *312*, 217; d) L. Cheng, K. Yang, S. Zhang, M. W. Shao, S. Lee, Z. Liu, *Nano. Res.* **2010**, *3*, 722; e) Q. Liu, Y. Sun, T. S. Yang, W. Fang, C. G. Li, F. Y. Li, *J. Am. Chem. Soc.* **2011**, *133*, 17122.

[13] a) V. J. Pansare, S. Hejazi, W. Faenza, R. K. Prud'homme, *Chem. Mater.* **2012**, *24*, 812; b) X.

H. Gao, Y. Y. Cui, R. M. Levenson, L. W. K. Chung, S. M. Nie, *Nat. Biotechnology* **2004**, *22*, 969.

[14] S. Diao, G. S. Hong, A. L. Antaris, J. L. Blacburn, K. Cheng, Z. Cheng, H. J. Dai, *Nano. Res.* **2015**, *8*, 580.

[15] G. S. Hong, Y. P. Zou, A. L. Antaris, S. Diao, D. Wu, K. Cheng, X. D. Zhang, C. Chen, B. Liu, Y. H. He, J. Z. Wu, J. Yuan, B. Zhang, Z. M. Tao, C. Fukunaga, H. J. Dai, *Nat. Commun.* **2014**, *5*, 4206.

[16] Z. M. Tao, G. S. Hong, C. Shinji, C. Chen, S. Diao, A. L. Antaris, B. Zhang, Y. P. Zou, H. J. Dai, *Angew. Chem. Int. Ed.* **2013**, *52*, 13002.

[17] A. L. Antaris, H. Chen, K. Cheng, Y. Sun, G. S. Hong, C. R. Qu, S. Diao, Z. X. Deng, X. M. Hu, B. Zhang, X. D. Zhang, O. K. Yaghi, Z. R. Alamparambil, X. C. Hong, Z. Cheng, H. J. Dai, *Nat. Mater.* **2016**, *15*, 235.

[18] a) O. T. Bruns, T. S. Bischof, D. K. Harris, D. Franke, Y. X. Shi, L. Riedemann, A. Bartelt, F. B. J aworski, J. A. Carr, C. J. Rowlands, M. W. B. Wilson, H. Wei, G. W. Hwang, D. M. Montana, L. Coropceanu, O. B. Achorn, J. Kloepper, J. Heeren, P. T. C. So, D. Fukumura, K. F. Jensen, R. K. Jain, M. G. Bawendi, *Nat. Biomed. Eng.* **2017**, *1*, 0056; b) Y. Zhang, G. S. Hong, Y. J. Zhang, G. C. Chen, F. Li, H. J. Dai, Q. B. Wang, *ACS Nano* **2012**, *6*, 3695; c) C. Y. Li, Y. J. Zhang, M. Wang, Y. Zhang, G. C. Chen, L. Li, D. Wu, Q. B. Wang, *Biomaterials* **2014**, *35*, 393; d) C. N. Zhu, P. Jiang, Z. L. Zhang, D. L. Zhu, Z. Q. Tian, D. W. Pang, *ACS Appl. Mater.*

Interfaces **2013**, *5*, 1186; e) G. S. Hong, J. T. Robinson, Y. J. Zhang, S. Diao, A. L. Antaris, Q. B. Wang, H. J. Dai, *Angew. Chem. Int. Ed.* **2012**, *51*, 9818.

[19] D. J. Naczynski, M. C. Tan, M. Zevon, B. Wall, J. Kohl, A. Kulesa, S. Chen, C. M. Roth, R. E. Riman, P. V. Moghe, *Nat. Commun.* **2013**, *4*, 2199.

[20] D. Kim, N. Lee, Y. I1. Park, T. Hyeon, *Bioconjugate Chem.* **2017**, *28*, 115.

[21] A. L. Rogach, A. Eychmuller, S. G. Hickey, & S. V. Kershaw, *Small* **2007**, *3*, 536.

[22] a) K. Welsher, Z. Liu, S. P. Sherlock, J. K. Robinson, Z. Chen, D. Daranciang, H. J. Dai, *Nat. Nanotechnol.* **2009**, *4*, 773; b) R. Wang, X. M. Li, L. Zhou, F. Zhang, *Angew. Chem. Int. Ed.* **2014**, *53*, 12086.

[23] a) J. Zhou, Q. Liu, W. Feng, Y. Sun, F. Y. Li, *Chem. Rev.* **2015**, *115*, 395; b) F. Wang, X. G. Liu, *Acc. Chem. Res.* **2014**, *47*, 1378; c) F. Wang, D. Banerjee, Y. S. Liu, X. Y. Chen, X. G. Liu, *Analyst.* **2010**, *135*, 1839; d) Y. S. Liu, D. T. Tu, H. M. Zhu, X. Y. Chen, *Chem. Soc. Rev.* **2013**, *42*, 6924; e) Z. G. Yi, X. L. Li, Z. L. Xue, X. Xiao, W. Lu, H. Peng, H. R. Liu, S. J. Zeng, J. H. Hao, *Adv. Funct. Mater.* **2015**, *25*, 7119; f) Y. L. Dai, H. H. Xiao, J. H. Liu, Q. H. Yuan, P. A. Ma, D. M. Yang, C. X. Li, Z. Y. Cheng, Z. Y. Hou, P. P. Yang, J. Lin, *J. Am. Chem. Soc.* **2013**, *135*, 4051; g) S. J. Zeng, Z. G. Yi, W. Lu, C. Qian, H. B. Wang, L. Rao, T. M. Zeng, H. R. Liu, B. Fei, J. H. Hao, *Adv. Funct. Mater.* **2014**, *24*, 4051; h) C. Li, *Nat. Mater.* **2014**, *13*, 110; i) W. Zheng, P. Huang, D. T. Tu, E. Ma, H. M. Zhu, X. Y. Chen, *Chem. Soc. Rev.* **2015**, *44*,1379; j) X. G. Liu, C. H. Yan, J. A. Capobianco, *Chem. Soc. Rev.* **2015**, *44*, 1299 ; k) Z. Liu, F. Pu, S. Huang, Q. H.

Yuan, J. S. Ren, X. G. Qu, *Biomaterials* **2013**, *34*, 1712.

[24] a) Z. J. Zhang, L. M. Wang, J. Wang, X. M. Jiang, X. H. Li, Z. J. Hu, Y. L. Ji, X. C. Wu, C. Y. Chen, *Adv. Mater.* **2012**, *24*, 1418; b) W. Y. Yin, L. Yan, J. Yu, G. Tian, L. Zhou, X. P. Zheng, X. Zhang, Y. Yong, J. Li, Z. J. Gu, Y. L. Zhao, *ACS Nano* **2014**, *8*, 6922; c) Z. J. Zhang, J. Wang, X. Nie, T. Wen, Y. L. Ji, X. C. Wu, Y. L. Zhao, C. Y. Chen, *J. Am. Chem. Soc.* **2014**, *136*, 7317.

[25] W. Han, L. X. Yi, N. Zhao, A. W. Tang, M. Y. Gao, Z. Y. Tang, *J. Am. Chem.* Soc. **2008**, *130*, 13152.

[26] B. Liu, C. X. Li, Z. X. Xie, Z. Y. Hou, Z. Y. Cheng, D. Y. Jin, J. Lin, *Dalton Trans.* **2016**, *45*, 13061.

[27] Q. F. Xiao, X. P. Zheng, W. B. Bu, W. Q. Ge, S. J. Zhang, F. Chen, H. Y. Xing, Q. G. Ren, W. P. Fan, K. L. Zhao, Y. Q. Hua, J. L. Shi, *J. Am. Chem. Soc.* **2013**, *135*, 13041.

[28] D. M. McDonald, P. L. Choyke, *Nat. Med.* **2003**, *9*, 715.

A general *in-situ* growth strategy of achieving integrative $NaLnF_4@Cu_{2-x}S$ theranostic nanoprobe combining efficient NIR-II emission and high performance PTT was demonstrated. NIR-II imaging guided small tumor diagnosis, non-invasive *in vivo* brain vessel imaging with high spatial resolution and PTT were achieved for the first time, providing a new opportunity of exploring highly sensitive theranostic nanoprobes integrating NIR-II imaging with PTT.

Mingyang Jiang, Xiaolong Li Zhenluan Xue, Youbin Li, Songjun Zeng, Hongrong Liu* and Jianhua Hao**

A rational design of $NaLnF_4@Cu_{2-x}S$ hybrid theranostic nanoplatform for *in vivo* through-skull brain imaging beyond 1500 nm and photothermal therapy.

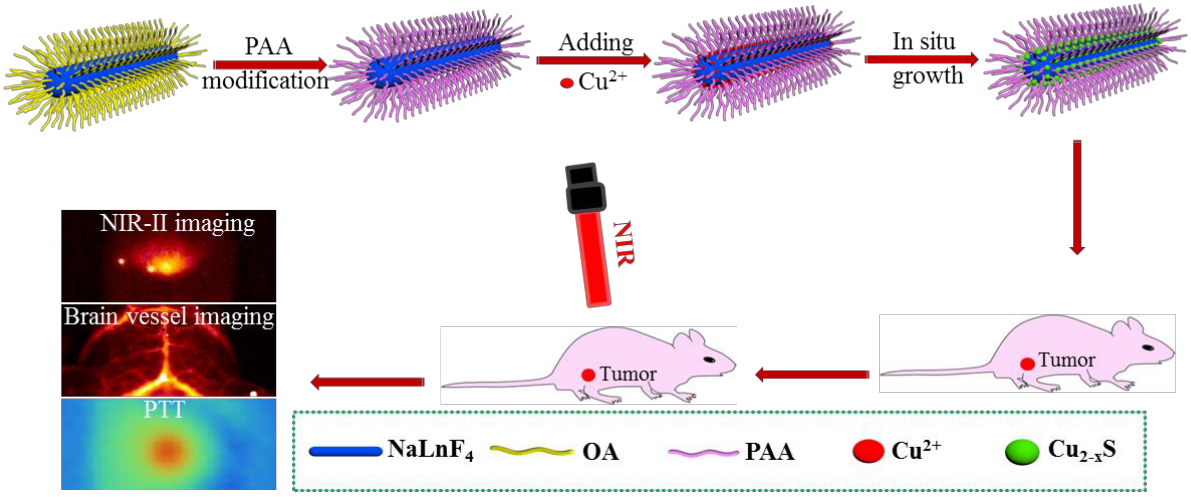

Supporting Information

A rational design of $NaLnF_4@Cu_{2-x}S$ hybrid therapeutic nanoplatform for *in vivo* through-skull brain imaging beyond 1500 nm and photothermal therapy.

Mingyang Jiang, Xiaolong Li, Zhenluan Xue, Youbin Li, Songjun Zeng, Hongrong Liu*and Jianhua Hao**

Prof. S. J. Zeng, M. Y. Jiang, Dr. X. L. Li, Z. L. Xue, Z. M. Deng, Prof. H. R. Liu

College of Physics and Information Science and Key Laboratory of Low-dimensional Quantum Structures and Quantum Control of the Ministry of Education, Synergetic Innovation Center for Quantum Effects and Applications, Hunan Normal University, Changsha, Hunan 410081 (China)

E-mail: ***songjunz@hunnu.edu.cn , hrliu@hunnu.edu.cn***

Prof. J. H. Hao

Department of Applied Physics, The Hong Kong Polytechnic University, Hong Kong (China)

E-mail: ***jh.hao@polyu.edu.hk***

Keywords: lanthanide nanomaterials, theranostic nanoprobes, NIR-II optical imaging, brain blood vessel imaging, photothermal therapy

Experimental Section

Materials: $YbCl_3 \cdot 6H_2O$ (99.9%), $ErCl_3 \cdot 6H_2O$ (99.9%), $YCl_3 \cdot 6H_2O$ (99.9%), $LuCl_3 \cdot 6H_2O$ (99.9%), and $GdCl_3 \cdot 6H_2O$ (99.9%) were obtained from Sigma-Aldrich. NaF, NaOH, ethanol, oleic acid (OA), poly acrylic acid (PAA), $CuCl_2 \cdot 2H_2O$, $Na_2S \cdot 9H_2O$, diethylene glycol (DEG), polyvinyl pyrrolidone (PVP) and other reagents were obtained from Sinopharm Chemical Reagent Co., China. All chemical reagents were used without any further purification.

Synthesis of OA-$NaLnF_4$: 20%Yb,50%Gd,2%Er: $NaLnF_4$ (Ln=Y, Lu, Yb) was prepared according to the reported literature.[S1] In a typical experiment process, 1.2 g NaOH and 2 ml water were added into the beaker under stirring until NaOH was completely dissolved. After that, 20 ml OA and 10 ml ethanol were added into the above solution, vigorously stirring until the water become homogeneous. Subsequently, 1 mmol rare earth chlorides were mixed with the above solution under stirring for 15 min. 8 mmol NaF water solution was then added to the solution. After 10 min stirring, the solution was transferred to the stainless Teflon-lined autoclave (50 mL) for reaction under 190℃ for 24 h. To remove residual solvents, the synthesized products were washed three times with ethanol and water for further application.

Synthesis of PAA-$NaLnF_4$: For further application, OA-$NaLnF_4$ was modified using PAA via ligand exchange method.[S2] Typically, 300 mg PAA and 30 ml DEG were mixed into a three-necked bottle and then heated to 110 °C. Under argon protection, the mixed solution was kept vigorously stirring until the PAA was completely dissolved. Then, the toluene and cyclohexane solution containing OA-$NaLnF_4$ was injected into the above solution and the temperature was kept

at 110 °C for 1 h. After that, the temperature was improved to 240 °C for 1.5 h. Finally, PAA modified $NaLnF_4$ was washed with ethanol and water.

In situ synthesis of $NaLnF_4$@$Cu_{2-x}S$ hybrid nanocomposite: 0.5 mmol PAA-$NaLnF_4$ was first dispersed in 10 ml deionized water, and then 0.1 mmol $CuCl_2$ was added. After 12 h stirring, the Cu^{2+} was successfully grafted on the surface of the PAA-$NaLnF_4$ nanorods owing to the electrostatic interaction. Then PVP was added with vigorously stirring until the PVP was completely dissolved. After that, 0.1 mmol Na_2S was added into the above solution under the room temperature for 5 min. Finally, the *in-situ* reaction was carried out by improving the temperature of the reaction mixture to 90 °C for 15 min. The resulting hybrid $NaLnF_4$@$Cu_{2-x}S$ nanocomposites were transferred to ice-water.

Characterization*:* The morphology and particle size of the synthesized $NaLnF_4$@$Cu_{2-x}S$ nanocomposites were characterized by transmission electron microscopy (TEM, FEI Tecnai F20), high resolution TEM (HRTEM) at 200 kV acceleration voltage. Upconversion (UC) luminescent spectra of the $NaLnF_4$@$Cu_{2-x}S$ nanocomposites were detected via a Zolix Analytical Instrument (fluoroSENS 9000 A) and the downconversion (DC) NIR-II fluorescence was recorded by using a NIR spectrometer (NIRQuest512, Ocean Optics) in the 900-1700 nm region under the excitation of 980 nm laser.

In vivo NIR-II real-time tracking and bio-distribution: The PAA-$NaYF_4$@$Cu_{2-x}S$ (150 μL, 2.0 mg/mL) was intravenously injected into the Kunming mouse to acquire NIR-II real-time tracking images, under the 980 nm laser for 11 h. The main organs, including heart, lung, spleen, liver and kidney, were separated from the same mouse, which was used to assess the biodistribution.

All of the low-magnification NIR-II images were taken through a home-made small animal NIR-II bioimaging system equipped with a thermoelectric cooled InGaAs camera (Model: NIRvanaTM Camera System, operating temperature: -80 ℃, Princeton Instruments, 512 × 640) with field of view (FOV) of 146 mm × 183 mm.

In vivo tumor detection by NIR-II fluorescence: The HeLa cells (1×10^6 cells/site) were subcutaneously injected into the Kunming mice as the tumor-bearing mice models, and the models were cultivated for several days. Subsequently, the PAA-$NaYF_4$@$Cu_{2-x}S$ nanoprobes (150 μL, 2.0 mg/mL) were intravenously injected into the tumor-bearing mouse via tail vein. NIR-II fluorescence imaging was also detected via the aforementioned imaging system at different time points. After *in vivo* imaging, the mouse was sacrificed and the tumor was dissected for *ex vivo* imaging and size evaluation.

In vivo non-invasive blood vessel imaging based on PAA-$NaYF_4$@$Cu_{2-x}S$ nanoprobes: To acquire more accurate blood vessel imaging, a high magnification NIR-II bioimaging with FOV of 26 mm × 21 mm was performed by using the same home-made imaging system under the excitation of the fiber-coupled 980 nm laser with power density of 100 mW/cm^2. The PAA-$NaYF_4$@$Cu_{2-x}S$ nanoprobes (150 μL, 2.0 mg/mL) were intravenously injected into the mouse, after the injection, the brain vessel imaging and abdomen blood imaging were immediately recorded by high-magnification NIR-II imaging.

In vivo photothermal therapy for ablating the cancer cells: The HeLa tumor-bearing mice were randomly divided into three groups. Group 1: PBS subcutaneous injection with 808 nm laser irradiation; Group 2: PAA-$NaYF_4$@$Cu_{2-x}S$ (150 μL 2 mg/mL) solution subcutaneous injection with

808 nm laser irradiation; Group 3: PAA-$NaYF_4$@$Cu_{2-x}S$ solution (150 μL 2 mg/mL) intravenous injection with 808 nm irradiation. The temperature increase was *in vivo* then monitored by FLUKE thermal camera under 808 nm irradiation for 10 min. Furthermore, the tumor-bearing mice were treated for 22 days with 808 nm laser irritation for 10 min every day.

Histological Assessment: To evaluate the *in vivo* toxicity, the main organs including heart, liver, spleen, lung and kidney from the untreated and treated for 3 and 7 days mice were collected for hematoxylin and eosin (H&E) staining to examine the potential side effect of PAA-$NaYF_4$@$Cu_{2-x}S$ nanoprobe. All animal experiments were in agreement with the institutional animal use and care regulations approved by the Laboratory Animal Center of Hunan Province.

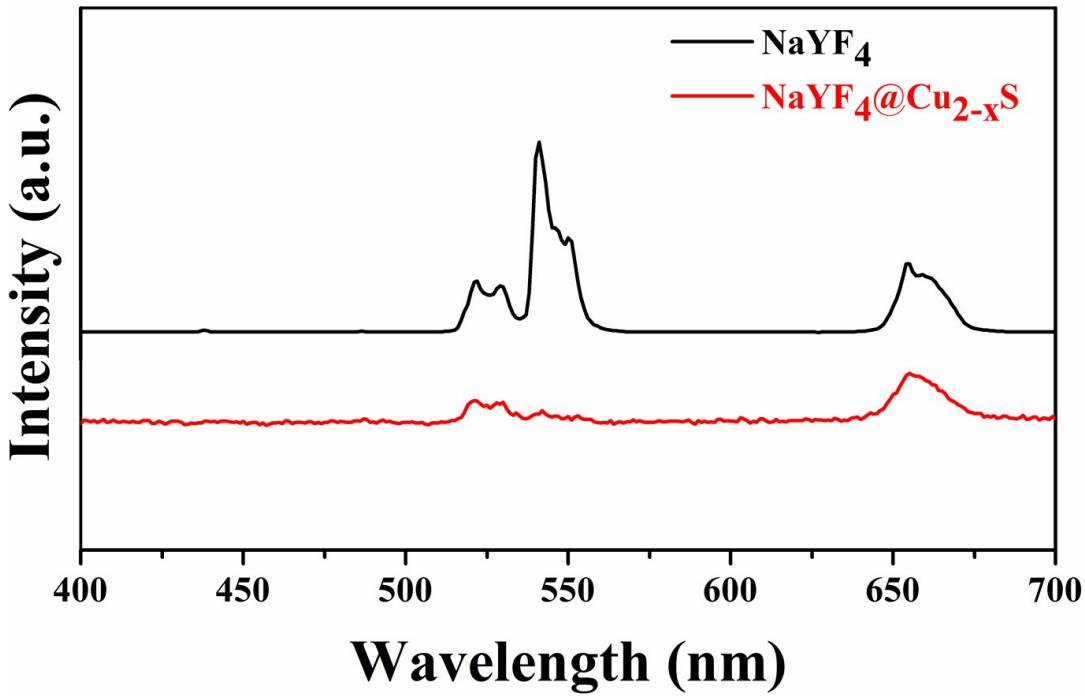

Supplementary Figure 1. UC optical emission of the $NaYF_4$:Gd/Yb/Er and $NaYF_4@Cu_{2-x}S$ nanocomposite in the NIR-I region.

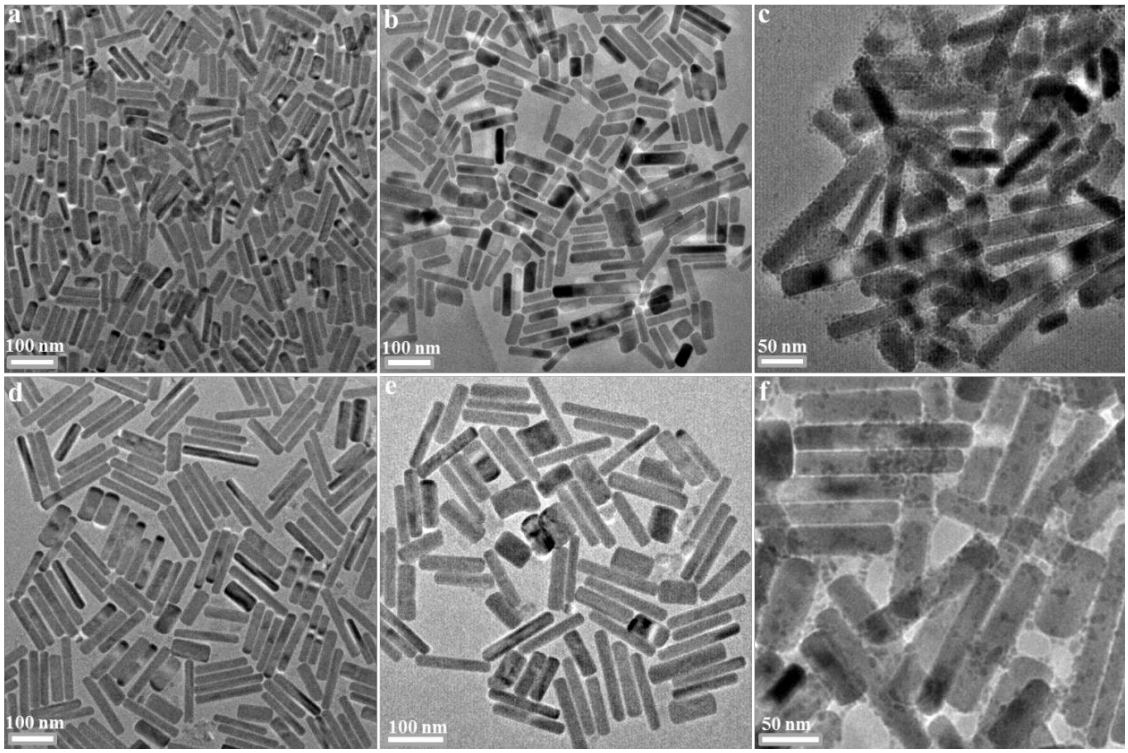

Supplementary Figure 2. (a) TEM image of the $NaLuF_4$ nanorods. (b) TEM image of the PAA-$NaLuF_4$ nanorods. (C) TEM image of the $NaLuF_4@Cu_{2-x}S$ hybrid nanocomposites. (d) TEM image of the $NaYbF_4$ nanorods. (e) TEM image of the PAA-$NaYbF_4$ nanorods. (f) TEM image of the $NaYbF_4@Cu_{2-x}S$ nanocomposites.

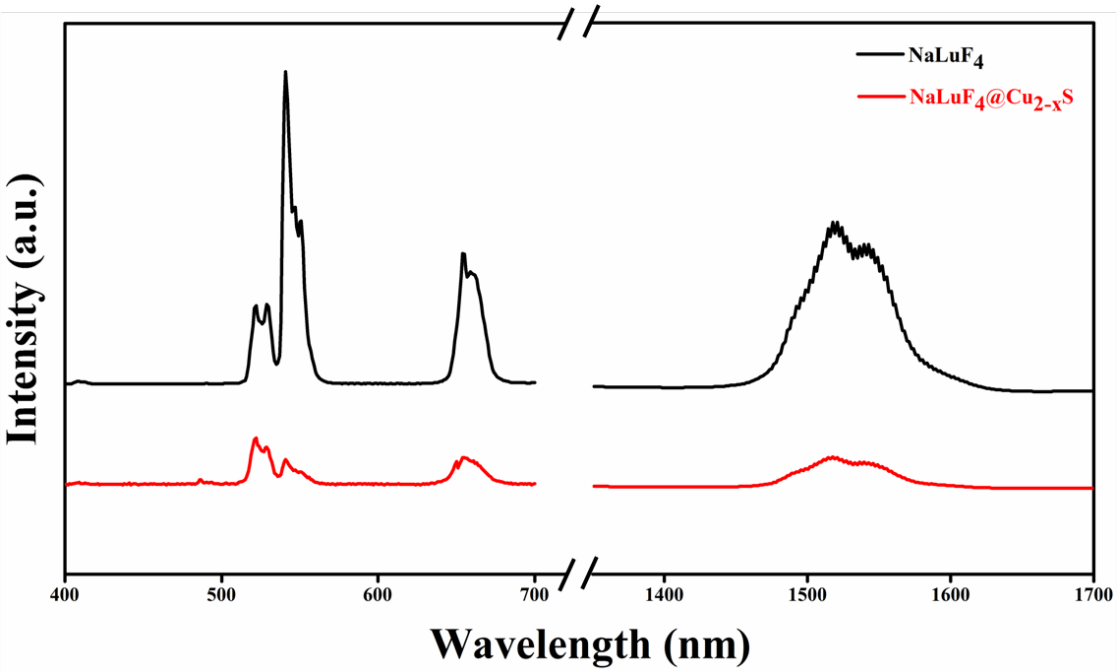

Supplementary Figure 3. Photoluminescence spectra of $NaLuF_4@Cu_{2-x}S$ spanning the visible (left, UC) and NIR-II (right, DC) regions under the excitation of 980 nm laser.

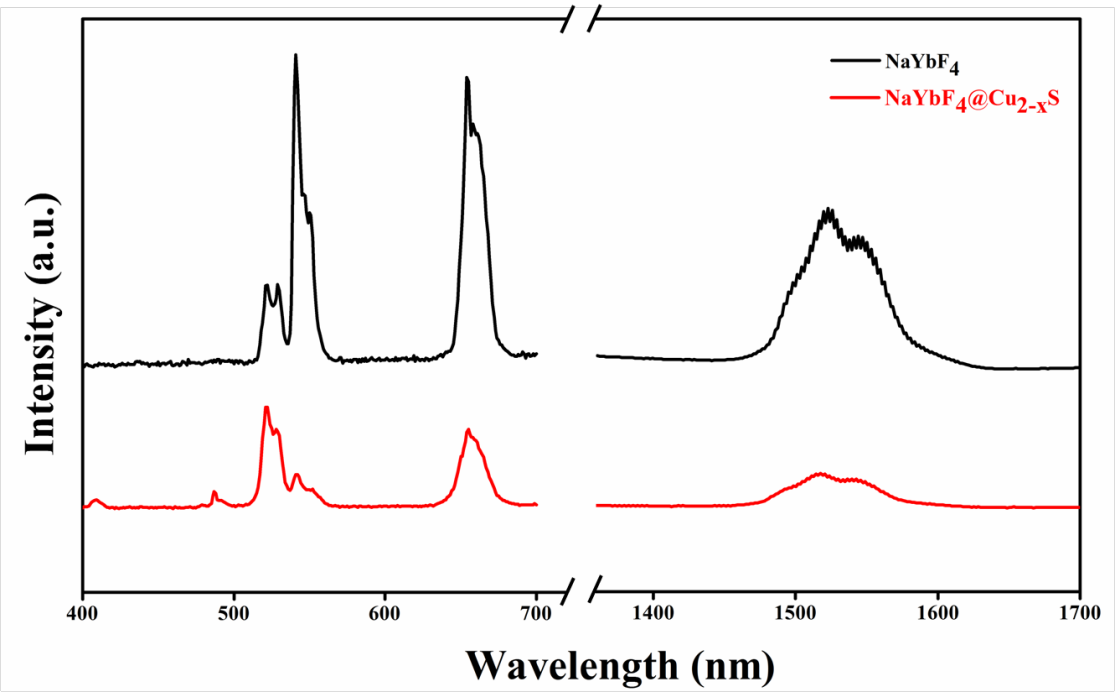

Supplementary Figure 4. Photoluminescence spectra of $NaYbF_4@Cu_{2-x}S$ spanning the visible (left, UC) and NIR-II (right, DC) regions under the excitation of 980 nm laser.

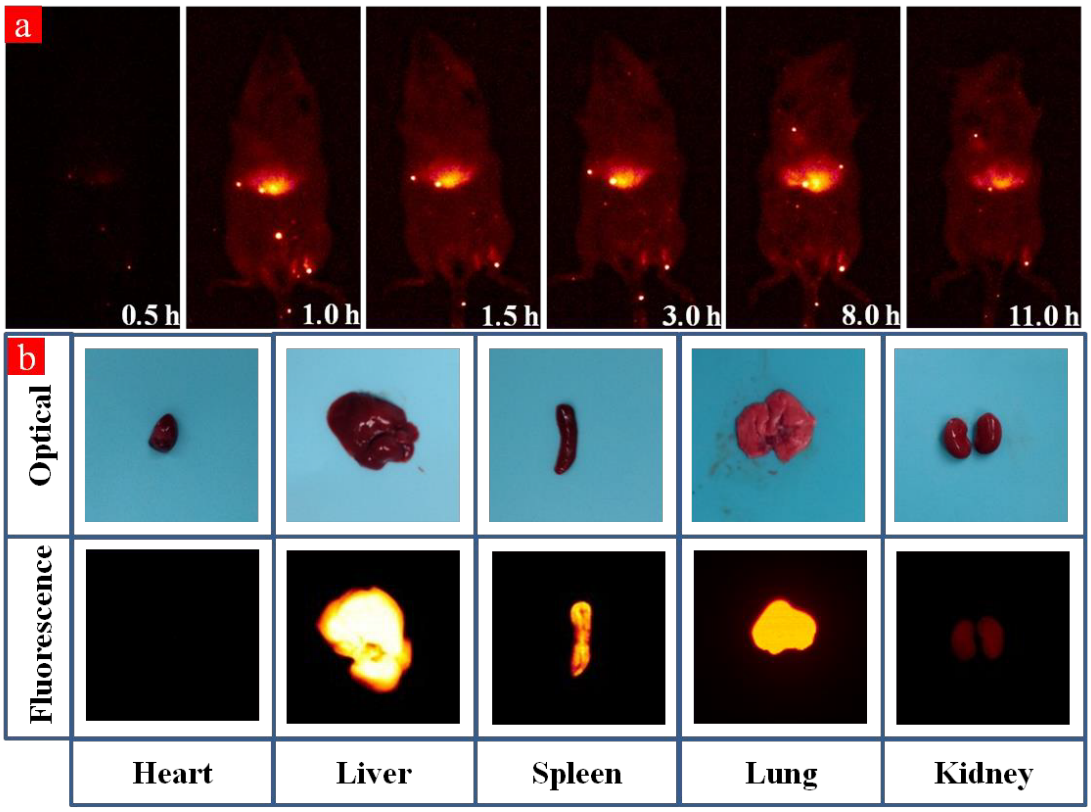

Supplementary Figure 5. (a) *In vivo* real time tracking. (b) Optical images and fluorescence images of the corresponding isolated organs, including the liver, spleen, heart, lung, and kidney from a sacrificed mouse after 11 h intravenous injection.

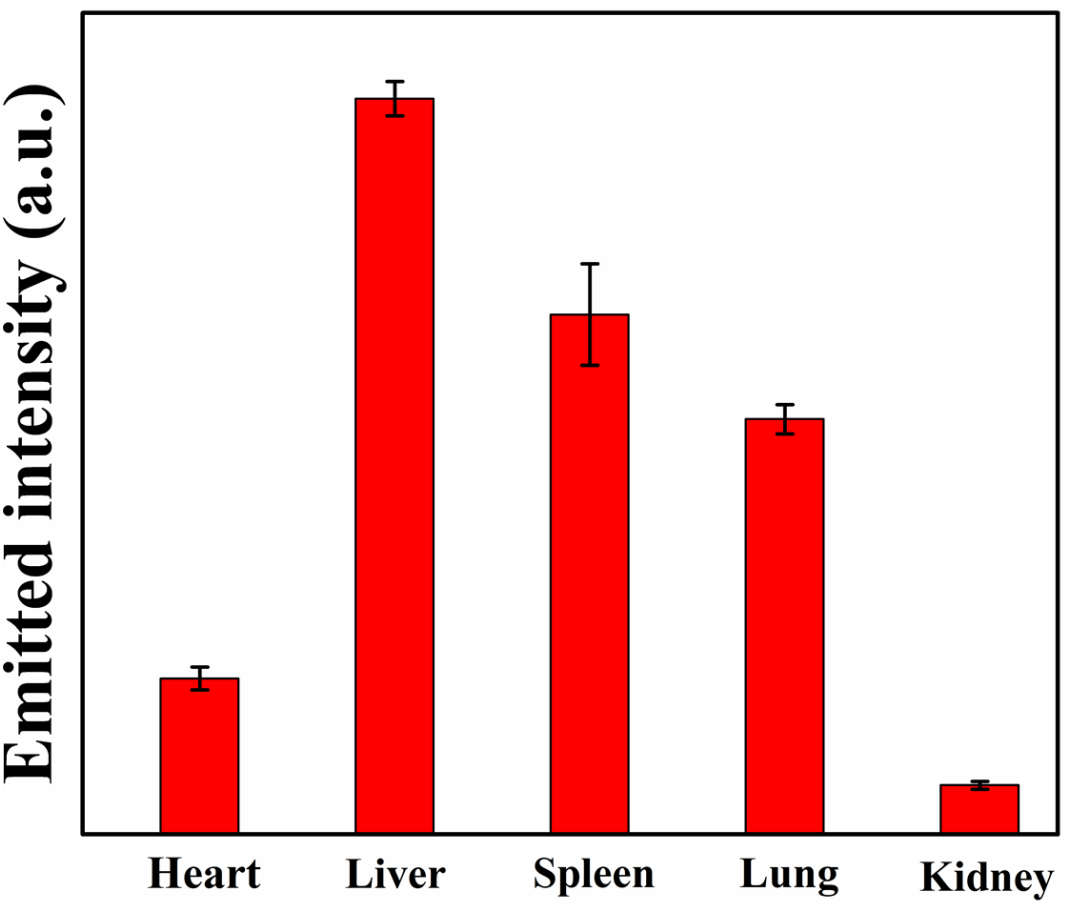

Supplementary Figure 6. Average signal intensity of various organs.

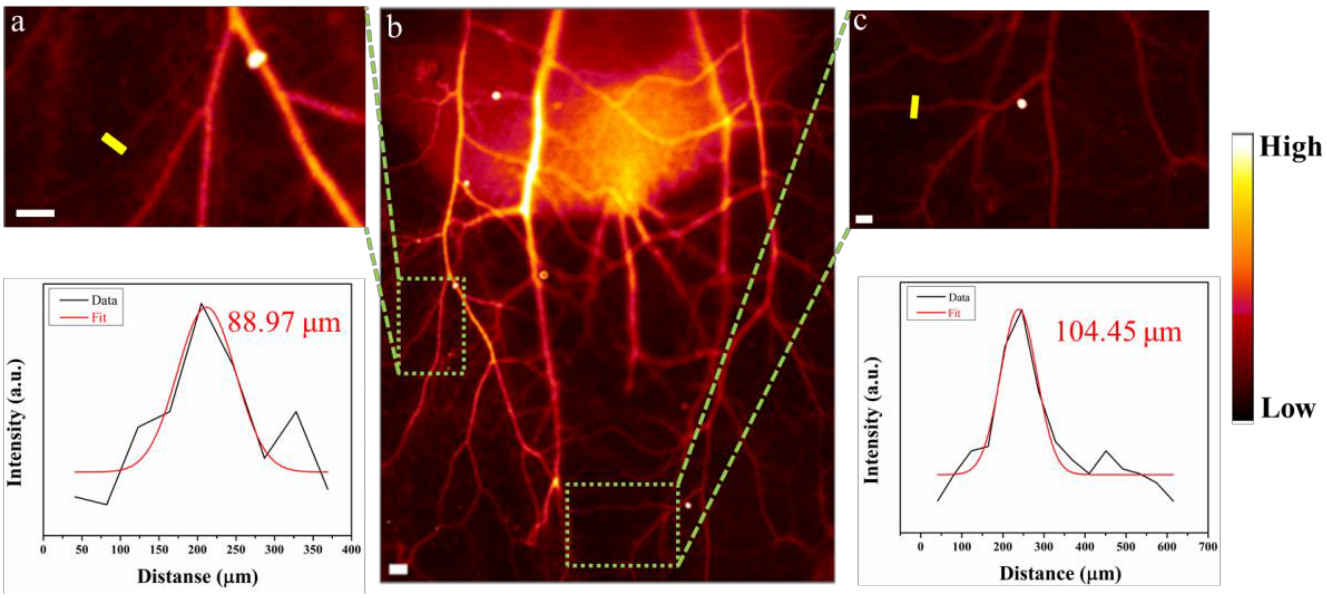

Supplementary Figure 7. (a,c) The enlarged NIR-II images of the mouse abdomen taken from the rectangle region of (b). (b) High-magnification abdomen image with a FOV of 21 mm × 26 mm. (Scale bar, 500 μm)

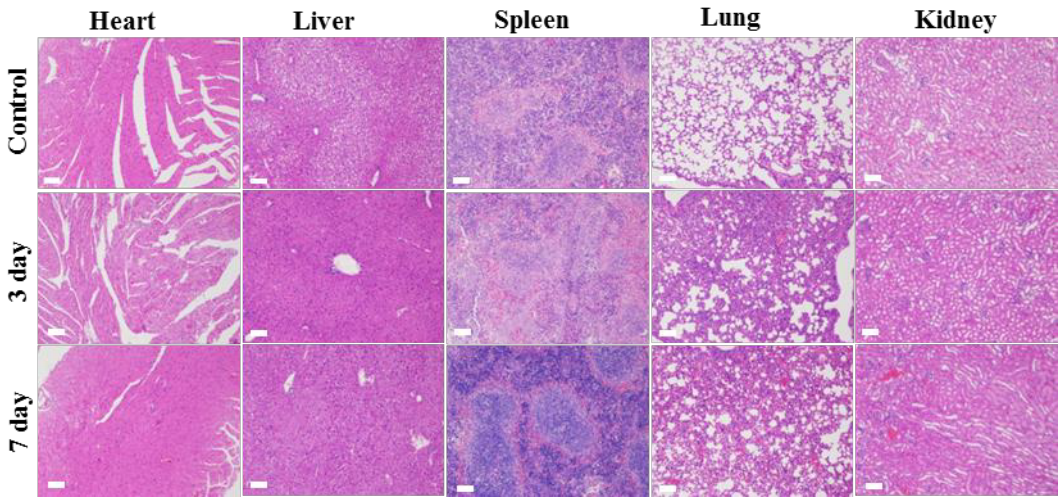

Supplementary Figure 8. H&E stained main tissues such as heart, liver, spleen, lung, and kidney collected from control mouse and mice treated with PAA-$NaYF_4$@$Cu_{2-x}S$ nanocomposites for 3 and 7 days. Scale bar = 100 μm.

[S1] F. Wang, Y. Han, C. S. Lim, Y. H. Lu, J. Wang, J. Xu, H. Y. Chen, C. Zhang, M. H. Hong, X. G. Liu, *Nature* **2010**, *463*, 1061.

[S2] T. R. Zhang, J. P. Ge, Y. X. Hu, Y. D. Yin, *Nano Lett.* **2007**, *7*, 3203.